JOURNAL OF PROPULSION AND POWER
Vol. 25, No. 1, January–February 2009

Effect of Recess in High-Pressure Liquid Oxygen/Methane Coaxial Injection and Combustion

Johannes Lux* and Oskar Haidn†
DLR, German Aerospace Center, 74239 Lampoldshausen, Germany

DOI: 10.2514/1.37308

The effect of a recessed liquid oxygen tube in shear coaxial injection has been investigated experimentally using an optically accessible subscale rocket combustor operated at pressures between 40 and 60 bar. Different single-shear coaxial injectors have been used to inject liquid oxygen and methane at relevant operating conditions covering sub-, near-, and supercritical pressures with respect to the critical point of oxygen. Liquid oxygen was injected at 120 K and the injection temperature of gaseous methane was about 275 K. Detection of spontaneous OH and CH chemiluminescence has been performed to characterize the flame-anchoring zone near the liquid oxygen post tip. In addition, the influence of the injector geometry on the combustion roughness and stability has been investigated during steady-state operating points. An increased flame expansion was observed with a recessed injector element. At a low momentum flux ratio, the pressure drop across the injector increases with a recessed liquid oxygen tube compared with a flush tube. Furthermore, a recessed liquid oxygen tube led to a smoother combustion in general; however, this configuration also led to additional resonant frequencies in the chamber acoustics.

Nomenclature

A	=	area, m^2
a	=	speed of sound, m/s
d	=	diameter, m
$\boldsymbol{e}_x$, $\boldsymbol{e}_y$	=	unit vectors in the x and y directions
f	=	frequency, Hz
G	=	magnitude of the gradient $\nabla \bar{I}_{\mathrm{OH}}$
I	=	emission intensity
J	=	momentum flux ratio
j	=	counter
K	=	coefficient
l	=	length, m
$\dot{m}$	=	propellant mass flow, kg/s
n	=	quantity
P	=	pressure, bar
Re	=	Reynolds number
ROF	=	propellant mixture ratio, $\dot{m}_{\mathrm{O_2}}/\dot{m}_{\mathrm{CH_4}}$
r	=	recess length, m
T	=	temperature, K
t	=	injector wall thickness, m
VR	=	velocity ratio
v	=	injection velocity, m/s
x	=	axial position, m
y	=	methane injection slot dimension, m
η	=	dynamic viscosity, Pa · s
ρ	=	density, kg/m^3

Subscripts

c	=	critical value
cc	=	combustion chamber
dyn	=	dynamic
g	=	gaseous
i, o	=	inner, outer
l	=	liquid
r	=	reduced value

Received 26 February 2008; accepted for publication 10 June 2008.

*Ph.D. Student, Research Engineer, Institute of Space Propulsion; johannes.lux@dlr.de. Member AIAA (Corresponding Author).

†Head of Technology, Institute of Space Propulsion. Associate Fellow AIAA.

I. Introduction

BECAUSE the propellant combination of liquid oxygen (LOX) and methane has become more attractive within the predevelopment of future launch vehicles, several groups have performed fundamental experimental and numerical investigations [1–5]. Today's liquid propellant rocket engines such as the space shuttle main engine (SSME) and the Vulcain II engine of the European Ariane 5 launcher are usually equipped with about 500–600 shear coaxial injector elements when operated with the cryogenic propellant combination LOX/H_2. With this type of injector, liquid oxygen is injected through an inner tube at velocities of about 20–30 m/s. The fuel is injected through an annulus gap at much higher velocities of about 200–400 m/s. Shear forces between both propellants lead to an instability of the liquid jet and finally to a disintegration into ligaments and droplets. Therefore, atomization characterizing dimensionless numbers such as the velocity ratio VR [Eq. (1)] and the momentum flux ratio J [Eq. (2)] take into account the relative motion of the two fluids:

$$\mathrm{VR} = \frac{v_g}{v_l} \tag{1}$$

$$J = \frac{(\rho \cdot v^2)_g}{(\rho \cdot v^2)_l} \tag{2}$$

It has been discovered from experiments in the past that recessing the LOX post with respect to the injection plane leads to a performance enhancement of the liquid propellant rocket engine. In this context, recess is defined as the axial distance r of the end of the inner tube to the injection plane. A recessed inner tube results in an improvement of the atomization and mixing [6]. Kendrick et al. [7] have shown that a recess of 1 d_i in subcritical LOX/H_2 combustion increases both the flame expansion rate and the diameter of the flame volume. At similar operating conditions and chamber pressures of 10 bar, Tripathi et al. [8] have reported that increasing the recess length above 1.5 d_i does not lead to further improvements. However, Wheeler and Kirby [9] have shown that a recess length of about 1.3 d_i in supercritical LOX/CH_4 combustion still leads to a further improvement in terms of combustion efficiency. Juniper and Candel [10] have demonstrated that a recess in LOX/H_2 combustion leads to self-sustained wakelike instabilities of the liquid jet.

It is well known from experimental investigations that modifications of injector geometries can lead to injection-coupled instability mechanisms [11]. Wanhainen et al. [12] and Hannum et al. [13] have demonstrated an improvement of combustion stability in subcritical LOX/H_2 combustion when using recessed injector elements. The hydrogen injection temperature at which the transition to an unstable combustion occurs decreased with increased recess of the injector LOX tubes. Stabilizing effects of a recessed LOX post have also been reported in LOX/kerosene investigations [14]. Mayer and Tamura [15,16] assumed that the recessed region of a coaxial injector can be regarded as a small combustion chamber that is insensitive to combustion disturbances in the main chamber. On the other hand, numerical simulations performed by Kim [17] and Kim et al. [18] have shown strong high-amplitude hydrodynamic instabilities in the recessed region of a coaxial injector under cold-flow conditions. Kim et al. assumed that these instabilities could influence the combustion stability of the engine. Self-pulsation has also been investigated experimentally by Bazarov and Yang [19]. Such hydrodynamic flow instabilities can lead to fluctuations of the liquid propellant distribution in the chamber and thus to combustion instabilities.

The present investigation deals with the near-injector flame structure and the combustion response of both nonrecessed and recessed single-shear coaxial injection of LOX/CH_4 at sub- to supercritical chamber pressures.

II. Experimental Configuration

All experiments have been performed at the European High-Pressure Research and Technology Test Facility P8 using the DLR, Germany Aerospace Center combustion chamber C, as shown in Fig. 1. The combustion chamber is water-cooled and has a total length of 430 mm with an inner diameter of 50 mm. A throat diameter of 17.3 mm has been chosen for the present investigation. Four quartz glass windows provide optical access to the near-injector region. A hydrogen film-cooling mass flow at ambient temperatures protects both the windows and the chamber walls from the hot gases during operation. The cooling mass flow has been regulated at 160–230 g/s to provide a constant injection velocity. It is supposed that the film-cooling mass flow does not influence the near-injector flame stabilization in a significant way. Nevertheless, an influence of the additional hydrogen on the combustion performance is presumed. A series of large eddy simulations of chamber C and combustion of LOX/hydrogen have been performed by Oefelein [20,21]. The influence of the window-cooling mass flow was analyzed numerically by Ivancic [22] and Ivancic and Mayer [23]. With methane as the window-cooling fluid, the required mass flow would have been even higher to meet the cooling demands.

Static and dynamic pressure transducers have been used at a data acquisition rate of 100 and 100 kHz, respectively. All pressure transducers have been calibrated and show errors of less than 0.25 bar in the area of interest [24]. The mass flows of liquid oxygen, gaseous hydrogen, and gaseous methane have been determined using flow turbines. Resulting mass flows have been determined with a density calculation using high-precision equations of state in the form of the Helmholtz free energy for oxygen and methane [25,26]. The density of hydrogen has been calculated using a modified Benedict–Webb–Rubin equation of state [27], which still represents the standard formulation for hydrogen in engineering applications [28]. The total resulting mass flow measurement error can be assumed to be less than 2%. High-precision temperature measurements are ensured by several thermocouples in the domes, in the chamber, and in the cooling-water supply system. The accuracy of the temperature measurement is ± 1.25 K [24]. Because it is not possible to measure the fluid temperatures shortly before entering the combustion chamber, injection conditions are calculated based on the combustion chamber pressure and the fluid dome temperatures. With this approach, heat transfer between the liquid oxygen and the methane within the injection element is neglected. To ensure maximum accuracy, all thermocouples, pressure transducers, and flow turbines have been individually calibrated.

Different single-shear coaxial injector elements have been used within the present study. The LOX post has an inner diameter d_i of 5.6 mm and a wall thickness t of 0.3 mm. Using an interchangeable nut, the methane injection diameter d_o was varied within a range of 7–8 mm. That allows a modification of the velocity ratio VR and the momentum flux ratio J without the need to adjust the mixture ratio or the mass flows. A typical injector element with a recessed LOX tube is shown in Fig. 2. A constant recess length r of 0.67 d_i has been chosen to maximize reproducibility. The total LOX-tube length of about 19–20 d_i ensures a well-established velocity profile. A metering orifice with an inner diameter of 2.2 mm is implemented at a position of about 1 d_i downstream of the inlet of the LOX post.

III. Optical Diagnostics

An identical pair of intensified high-speed charge-coupled-device cameras (Photron FASTCAM Ultima APX I^2) is used to detect spontaneous OH and CH chemiluminescence. Both systems are equipped with a 10-bit CMOS (complementary metal-oxide-semiconductor) sensor and an appropriate UV image intensifier. A typical optical setup is shown in Fig. 3. Both camera heads were fitted with a fixed focal length of 105 mm, a 1:4.5 Nikon Nikkor UV lens, and a relevant narrow bandwidth filter. OH emission was detected at 308 nm $\pm$ 5 nm and CH emission was detected at 430 nm $\pm$ 3 nm. The cameras have been set up at the same distance from the

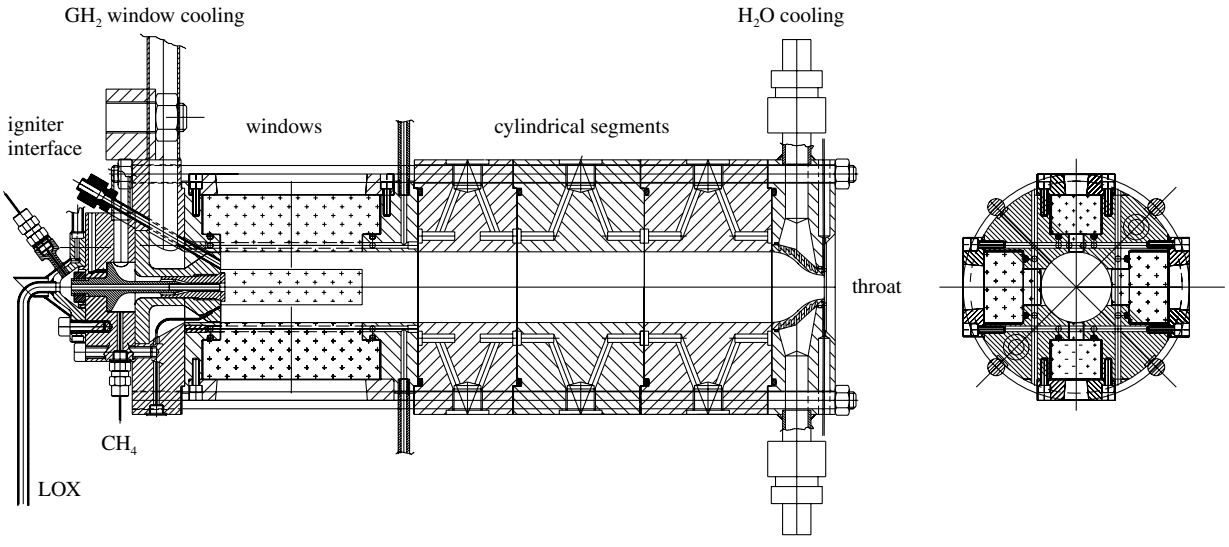

Fig. 1 Combustion chamber C with window segment and single-shear coaxial injector element.

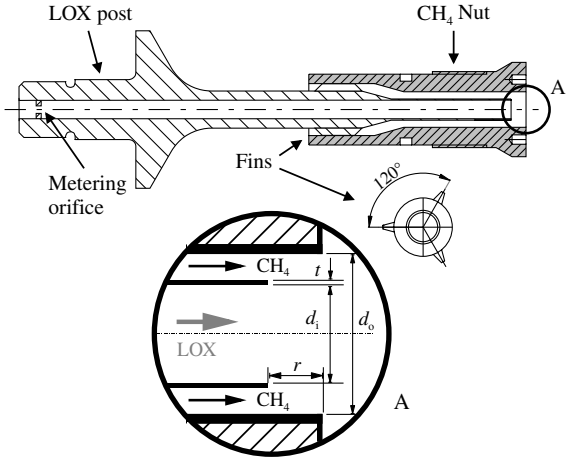

Fig. 2 Single-shear coaxial injector element with a recessed LOX post.

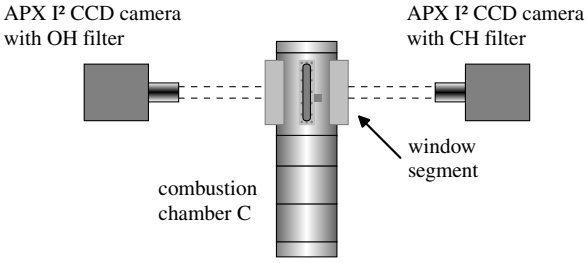

Fig. 3 Optical setup for emission imaging.

combustion chamber to get a similar optical resolution. As a result, both cameras can be used for either CH and OH emission detection or just OH emission detection at different time intervals. Flame emission was detected at a frame rate of 8 kHz with a resulting optical resolution of 1024×256 pixels covering the full window area of 100×25 mm^2. That turned out to be a good compromise between a high optical resolution and a relatively long recording time during the different operating points. To cover the full dynamic range of the system, the exposure time has been fixed at 10 μs, which represents the best-possible instantaneous emission images.

All emission images have been analyzed using different processing techniques. Time-averaged images have been calculated out of 8192 single shots each, representing 1.024 s total recording time. High-speed analysis has been performed using the original 10-bit format and different threshold algorithms in combination with noise reduction to focus on the relevant aspects. With the assumption of an axisymmetric flame, a deconvolution according to Abel's method has been performed using a computer code based on the theory published by Ostrovskii et al. [29]. Herding et al. [30] have successfully demonstrated the application of this technique to subcritical LOX/hydrogen flames. Noise reduction of deconvolved images has been conducted using a 3×3 pixel adaptive Wiener filter as described by Pham [31]. Especially in the injector near field, an Abel transformation provides information about the dimensions of the reaction zone between the liquid oxygen and the gaseous methane.

Gradients of the relative emission intensity sometimes indicate details that are not clearly visible in the false-colored averaged images (e.g., the flame-anchoring position at the LOX post tip). For that purpose, the magnitude of the gradient $\nabla \bar{I}_{\mathrm{OH}}$ of the averaged OH emission,

$$G(x,y) = \left(\left(\frac{\partial I_{\mathrm{OH}}(x,y)}{\partial x} \boldsymbol{e}_x \right)^2 + \left(\frac{\partial I_{\mathrm{OH}}(x,y)}{\partial y} \boldsymbol{e}_y \right)^2 \right)^{1/2} \tag{3}$$

has been calculated for different time-averaged emission images.

Table 1 Typical operating conditions

	Phase 1	Phase 2	Phase 3
P_r	1.18	1.00	0.80
T_{LOX}, K	120.2	121.1	123.9
$T_{\mathrm{CH_4}}$, K	282.6	279.9	277.2
ROF	3.40	3.42	3.36
$\dot{m}_{\mathrm{LOX}}$, g/s	302.4	253.0	201.9
$\dot{m}_{\mathrm{CH_4}}$, g/s	89.03	74.01	60.02
v_{LOX}, m/s	12.32	10.40	8.50
$v_{\mathrm{CH_4}}$, m/s	90.92–230.2	89.75–227.3	92.06–230.7
VR	7.44–19.33	8.63–22.67	10.83–28.38
J	2.69–16.92	3.10–19.68	3.95–25.04
ΔP_{LOX}, % P_{cc}	40.0–44.2	33.5–36.9	27.7–30.2
$\Delta P_{\mathrm{CH_4}}$, % P_{cc}	5.90–49.9	5.41–47.6	6.58–49.6

IV. Operating Conditions

In conformance with former investigations, the combustion chamber has been operated at three steady-state operating points representing sub-, near-, and supercritical conditions [4,32]. The operating sequence has been divided into three phases. The reduced pressure P_r is defined as the ratio of the combustion chamber pressure to the critical pressure of oxygen:

$$P_r = P_{\mathrm{cc}} / P_{\mathrm{c,O_2}} \tag{4}$$

Phase 1 represents supercritical conditions at about 60 bar ($P_r > 1$), phase 2 ($P_r \approx 1$) refers to near-critical conditions, and phase 3 ($P_r < 1$) covers the subcritical conditions. The mixture ratio ROF was kept constant at 3.4 throughout all tests. Similar to former investigations [4,33], liquid oxygen was injected at 120 K. With a critical temperature of 154.581 K and a critical pressure of 50.43 bar [25], oxygen is injected in a subcooled state, typical for LOX/H_2 rocket engines. Gaseous methane was maintained at about 275 K. Table 1 shows typical operating conditions during all three phases. Because the methane injection velocity, the velocity ratio, and the momentum flux ratio depend on the variable injection diameter d_o, the full ranges are given in Table 1.

V. Experimental Results

A. Near-Injector Flame Shape

Five different injector geometries, each one without and with recess ($r = 0.67 d_i$), have been investigated intensively. It turned out that there is only a small difference between OH and CH emission in both instantaneous and averaged images. A typical pair of normalized averaged OH emission images taken during phase 1 (supercritical conditions) is shown in Fig. 4. In both cases, the flame surrounds the liquid oxygen jet for the first 4–6 d_i. In the case of the nonrecessed LOX tube, the expansion angle of the jet is smaller than in the case of the recessed tube. The images also indicate that the total flame emission right after injection is stronger with recess. That can be related to a better initial atomization and mixing. After an axial

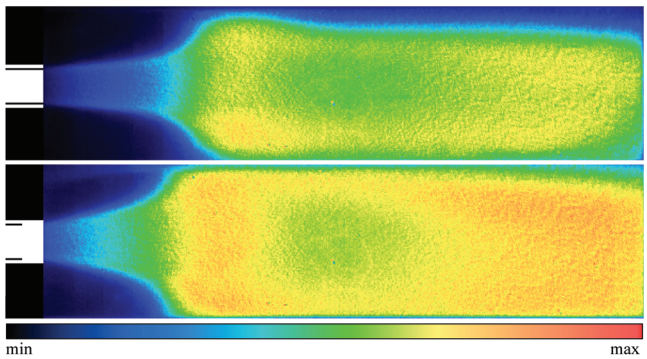

Fig. 4 Averaged OH emission (100×25 mm^2) taken during phase 1 ($P_r > 1$); injector without recess (top) and with recess (bottom); $d_o = 7.4$ mm.

distance of 4–6 d_i, the flame expands and partially exceeds the radial dimension of the windows in the case of the recessed LOX tube. The total flame volume within the optically accessible area seems to be larger in the case of a recess. This effect is visible during all operating pressures and is in conformance with LOX/H_2 investigations performed by Kendrick et al. [7].

Figure 5 shows a 33.5 × 25 mm^2 cutout of the near-injector region of the emission images shown in Fig. 4. All image intensities have been normalized to cover the full color scale. Figure 5b shows an Abel transformation of the time-averaged OH emission images, and Fig. 5c shows the magnitude of the gradient. In the case of the deconvolved images, the normalization has been performed in such a way that maximum intensity is reached within the shear layer right after injection. Therefore, total intensities of deconvolved images should not be compared with each other. It can be assumed from the images that the flame anchors in the wake of the LOX post tip in both cases. In the case of a recessed LOX tube, the reacting shear layer between liquid oxygen and gaseous methane is thicker. That could indicate an anchoring of the flame inside the recessed region. This is particularly visible from the OH emission profiles shown in Fig. 6. Time-averaged OH emission images, as shown in Fig. 5a, have been equalized by subtraction of the background emission intensity that was detected at the position of the injector nut. The normalized OH emission intensity, as shown in Fig. 6, represents the total intensity of every single column of the time-averaged images. In the case of the injector with recess, emission intensity starts at a higher level shortly behind the methane injection nut, which means that the axial gradient is much higher (as shown in Fig. 5c). That in turn leads to the conclusion that the flame is anchored inside the recessed region.

The near-injector region of all images has been analyzed using an adaptive edge-detection algorithm to quantify the flame expansion. It

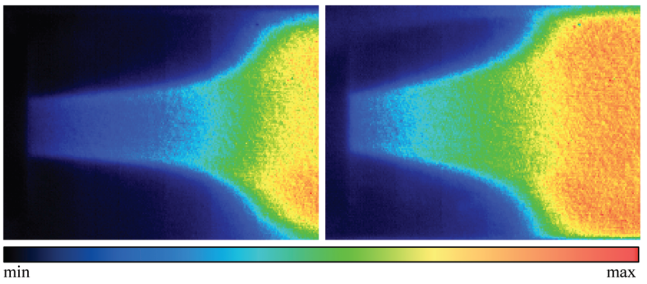

a) Time-averaged OH emission

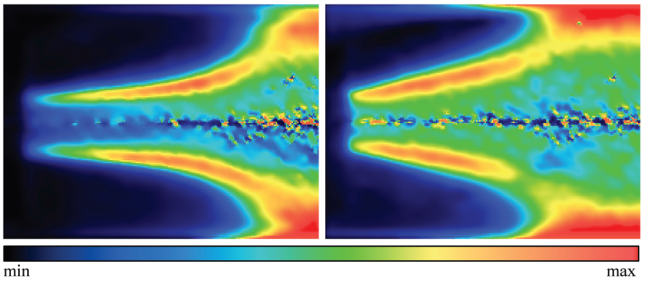

b) Deconvolved time-averaged OH emission

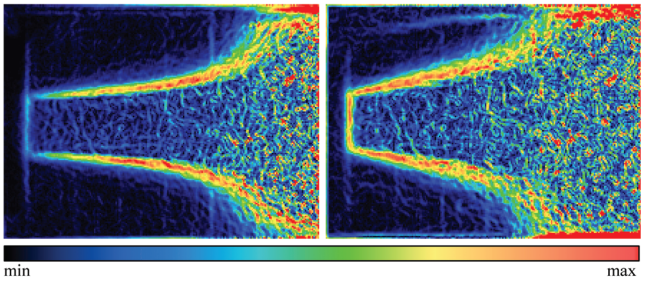

c) Magnitude of the gradient $\nabla \bar{I}_{OH}$

Fig. 5 OH emission images of the near-injector zone (33.5 × 25 mm^2); injector without recess (left) and with recess (right); d_o = 7.4 mm.

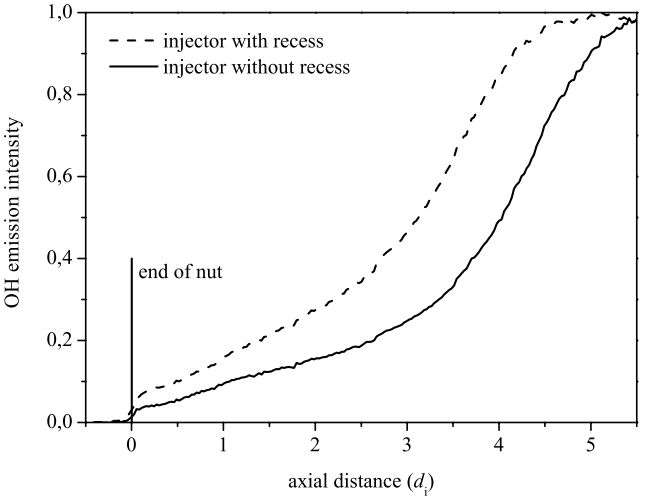

Fig. 6 Normalized time-averaged OH emission intensity as a function of the axial distance.

has been found that the near-injector flame expansion can be correlated to the momentum flux ratio. Figure 7 shows the jet diameter as a function of the momentum flux ratio J at three different axial positions downstream of the injector face. In this context, the jet diameter is defined as the diameter of the visible jet in the averaged OH emission images, detected using a threshold technique. In the case of a nonrecessed LOX tube, the expansion slightly decreases with increasing momentum flux ratio, as shown in Fig. 7a. With a

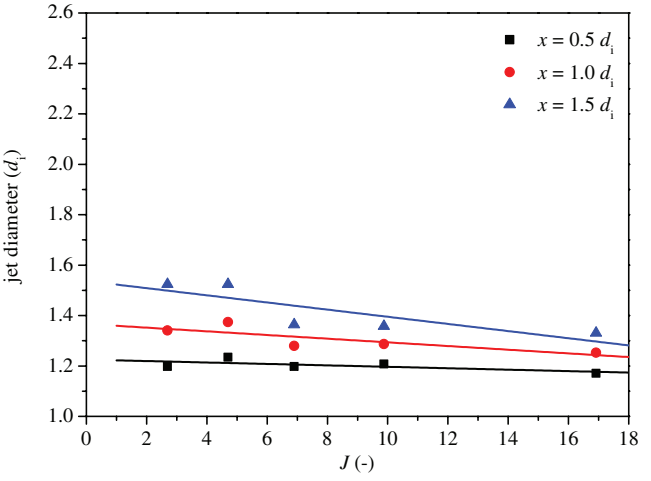

a) Injector without recess, phase 1 ($P_r > 1$)

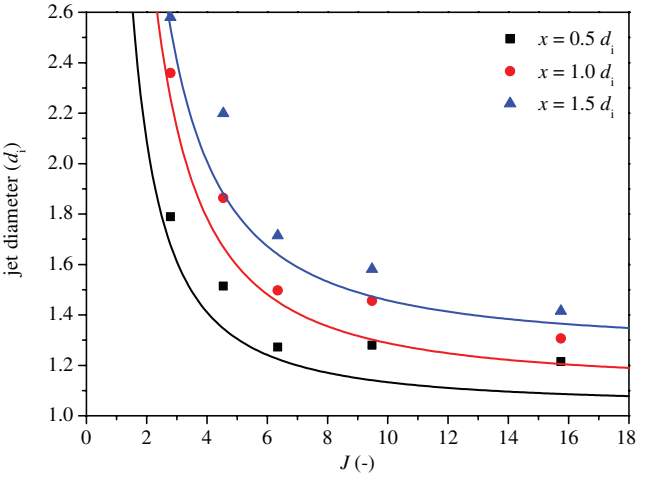

b) Injector with recess $r = 0.67\ d_i$, phase 1 ($P_r > 1$)

Fig. 7 Jet diameter as a function of J at different axial distances x.

recessed LOX tube, the flame expansion increases strongly with decreasing J. Figure 7 refers to phase 1 ($P_r > 1$), but the trend is generally visible throughout all operating conditions.

B. Pressure Loss Across the Injector

Experimental cold-flow investigations using water and gaseous nitrogen have recently been conducted by Nunome et al. [34]. It has been shown that the momentum of the gaseous jet influences both the liquid and the gaseous discharge coefficients of a recessed coaxial injector element. Because the flame is believed to anchor inside the recessed region in hot-fire conditions [15], a strong influence on the pressure loss across the injector $\Delta P = P_{\text{dome}} - P_{\text{cc}}$ can be assumed. The reacting shear layer is possibly thicker than the LOX-tube wall thickness. That in turn leads to a reduction of both the oxygen and the methane injection area at the injector face. Two coefficients K_{CH_4} and K_{LOX} have been defined as

$$K_{\text{CH}_4} = \frac{(\Delta P_{\text{CH}_4})_{\text{recess}} - \Delta P_{\text{CH}_4}}{\Delta P_{\text{CH}_4}} \tag{5}$$

$$K_{\text{LOX}} = \frac{(\Delta P_{\text{LOX}})_{\text{recess}} - \Delta P_{\text{LOX}}}{\Delta P_{\text{LOX}}} \tag{6}$$

Figure 8 shows the variation of the injector-side pressure loss as a function of the momentum flux ratio J. Because the LOX injection velocity has not been changed at the same pressure levels, J corresponds with the total momentum flux of the methane. Because

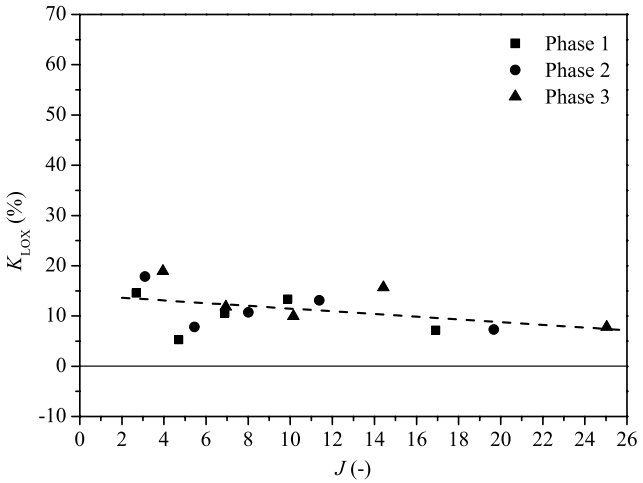

a) LOX-sided pressure loss variation

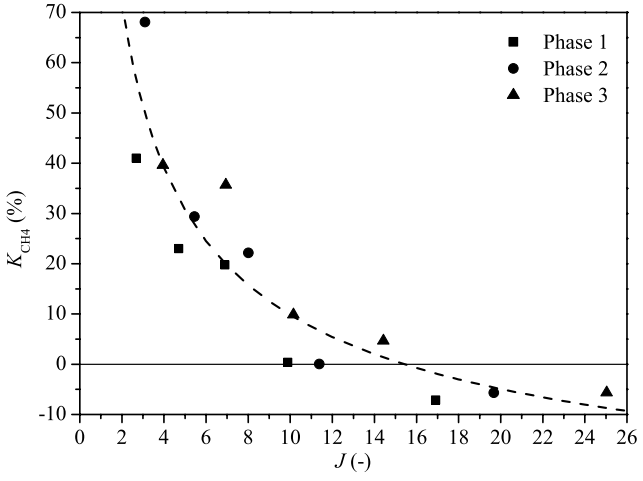

b) CH_4-sided pressure loss variation

Fig. 8 Variation of the pressure loss across the injector.

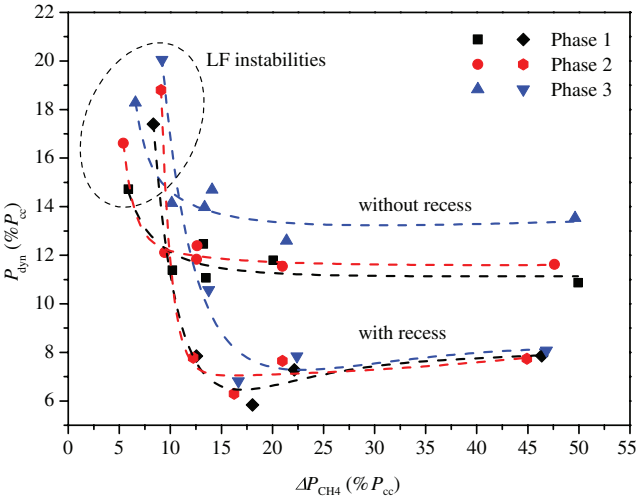

Fig. 9 Combustion roughness as a function of ΔP_{CH_4} (LF denotes low frequency).

of the measurement accuracy, no differentiation between the three operating phases has been done for the curve fit. As shown in Fig. 8a, the LOX-side pressure loss during a hot run is about 10% higher with a recessed LOX tube. Thus, it can be assumed that the flame inside the recessed region confines the oxygen inlet area.

This effect is more strongly developed on the methane-injection side, as shown in Fig. 8b. A recessed LOX tube leads to a much higher pressure loss at low momentum flux ratios J. Above $J \approx 15$ the effect even turns around so that the pressure loss is smaller with a recessed LOX tube than with a nonrecessed one. The data represent a comparison of different hot runs and should be handled with care. Even with the high repeatability of the test bench, small variations in the injection temperatures could influence the pressure data.

C. Combustion Roughness

When pressure fluctuations during steady-state operation exceed about $\pm 5\%$ P_{cc}, the combustion is called *rough* [35]. It is known that recessing the injector LOX tube can increase an engine's stability margin. Figure 9 shows the average dynamic pressure in terms of the static chamber pressure as a function of the fuel-side pressure drop across the injector. The relatively high level of combustion roughness should not be overrated because it may be due to the special combustion chamber characteristics. A massive window-cooling mass flow, the single injector element, and a contraction ratio of $A_{\text{cc}}/A_{\text{throat}} = 8.4$ are believed to support combustion roughness in LOX/H_2 combustion as well.

Nevertheless, it is evident from Fig. 9 that the combustion roughness decreases with a recessed LOX tube. It is also visible that a pressure drop across the fuel side below about 10–12% of the chamber pressure leads to a low-frequency instability (chugging). Recessing the LOX tube slightly increases the critical pressure drop so that a recessed injector earlier tends to a chugging instability when lowering the pressure drop.

D. Near-Injector Jet Dynamics

High-speed OH emission images taken at the near-injector region of a recessed single-shear coaxial injector show a strong dynamic of the LOX jet surface. Although the averaged images only provide an insight into the mean flame shape, the single shots offer a high temporal resolution.

Figure 10 shows two sets of the OH emission within an area of 33.5×25 mm^2 of the near-injector region during phase 1 (left column) and phase 3 (right column). All images have been taken during normal steady-state operation at a very low combustion roughness. Because the reacting shear layer surrounds the liquid jet right after injection, it can be assumed that these fluctuations refer to the surface of the liquid oxygen jet. It has been found that the

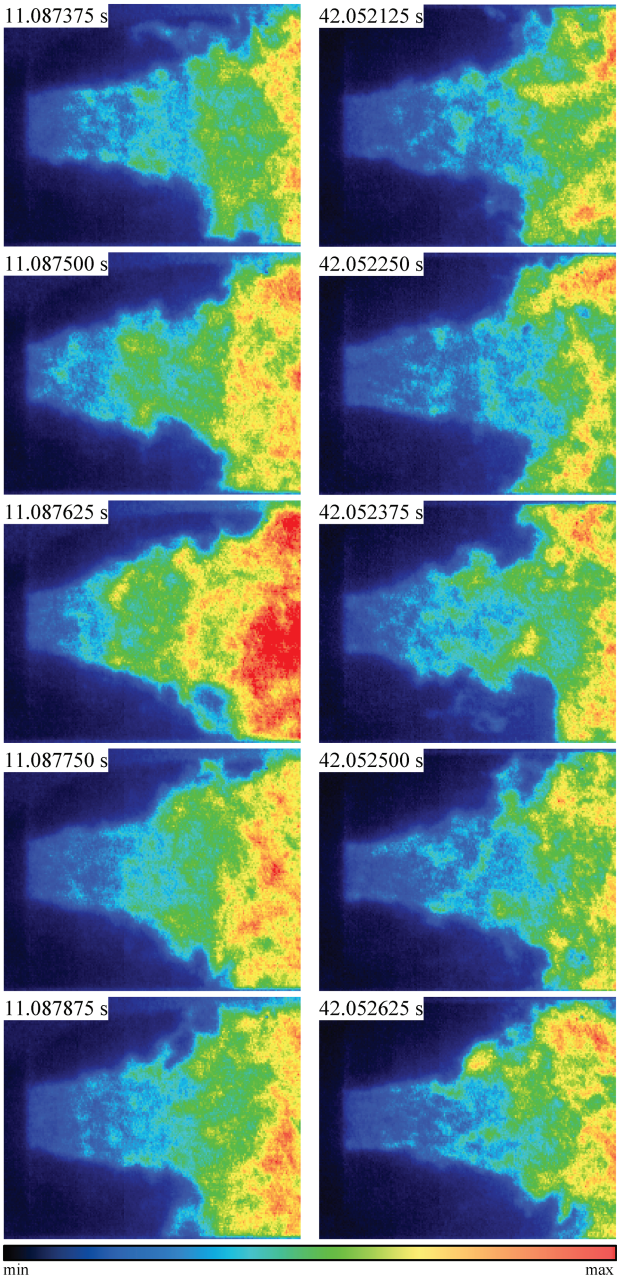

Fig. 10 OH emission cutoff (33.5 × 25 mm²); fluctuations on the LOX jet surface during phase 1 (left) and phase 3 (right); $\Delta t = 1.25 \times 10^{-4}$ s.

fluctuations appear suddenly for a limited time interval. In addition, they appear more often at supercritical conditions (phase 1) than at subcritical conditions (phase 3). No fluctuations on the surface of the LOX jet are visible at operation using a nonrecessed injector. The effect is also visible in Fig. 11, which represents the normalized variance of the OH emission intensity in the near-injector region (20×25 mm^2). The jet edges of 50 consecutive OH emission images are shown in Fig. 12 for both a nonrecessed and a recessed injector. It becomes apparent from these images why the flame spreading angle is larger with a recessed LOX tube, as shown in Figs. 4 and 5.

E. Combustion Chamber Acoustics

Because of the large length-to-diameter ratio of combustion chamber C, the frequencies of the first five longitudinal modes are below 10 kHz. According to [36], they are given by

$$f_{\text{theoretical}} = \frac{j \cdot \bar{a}}{2 \cdot l_{cc}} \tag{7}$$

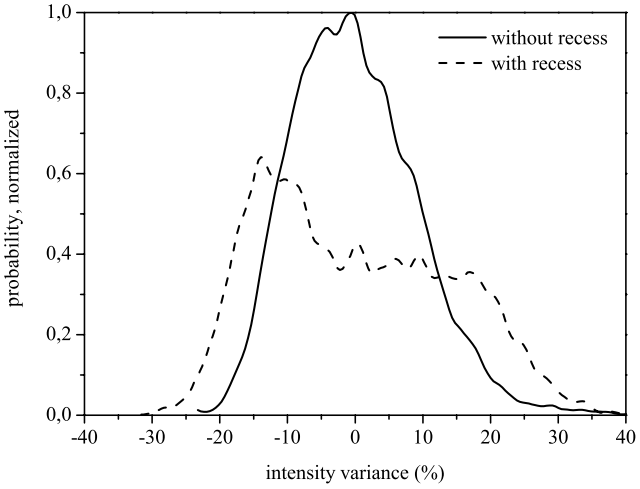

Fig. 11 Normalized variance of the OH emission intensity.

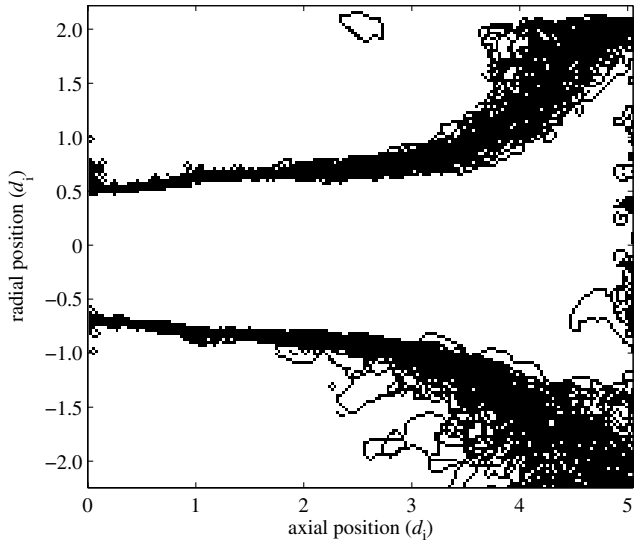

a) Without recess

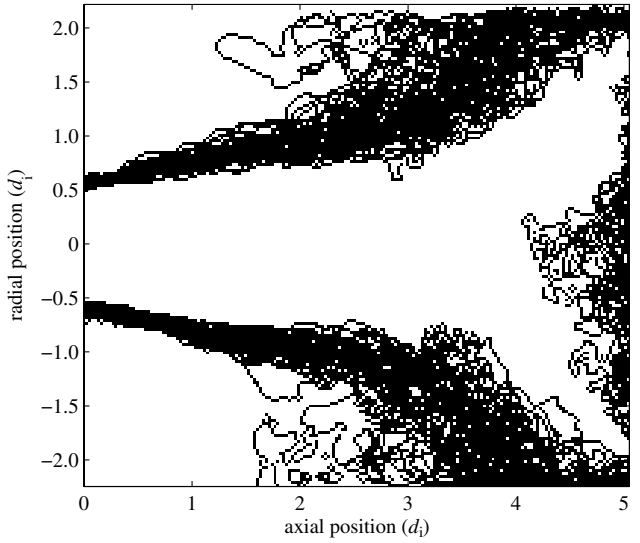

b) With recess

Fig. 12 Comparison of the near-injector jet edges of $n = 50$ consecutive OH emission images during phase 1 ($P_r > 1$).

Table 2 Longitudinal modes of chamber C, l_{cc} = 430 nm

Mode	j	$f_{theoretical}$	$f_{measured}$	Deviation
1L	1	1907	1820	−4.78%
2L	2	3814	3810	−0.10%
3L	3	5721	5670	−0.90%
4L	4	7628	7490	−1.84%
5L	5	9535	9270	−2.86%

where $j = 1, 2, 3, \ldots$, a mean speed of sound of $\bar{a} = 1640$ m/s [37], and the calculated and measured frequencies are given in Table 2. A typical power spectrum, including the longitudinal modes 1L–5L, is shown in Fig. 13a. It has been calculated using Welch's method [38] in combination with Hamming windows. An additional peak at about 6300 Hz is believed to be vortex shedding at the hydrogen film-cooling inlet [24].

Different power spectra of hot runs using an injector without (left column) and with (right column) a recessed LOX tube are given in Fig. 13. It can be seen that in the case of a recessed LOX tube,

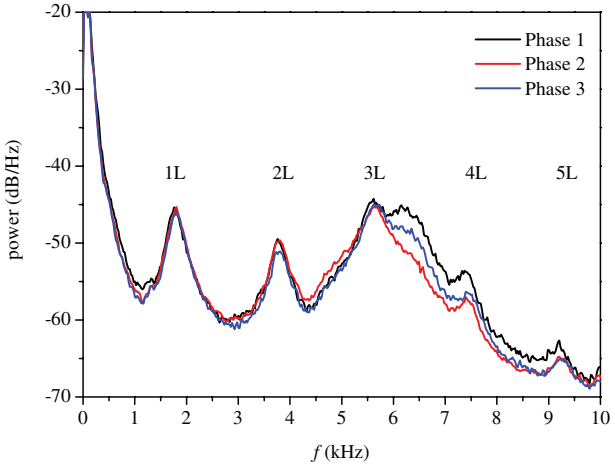

a) Point A: d_o = 7.0 mm

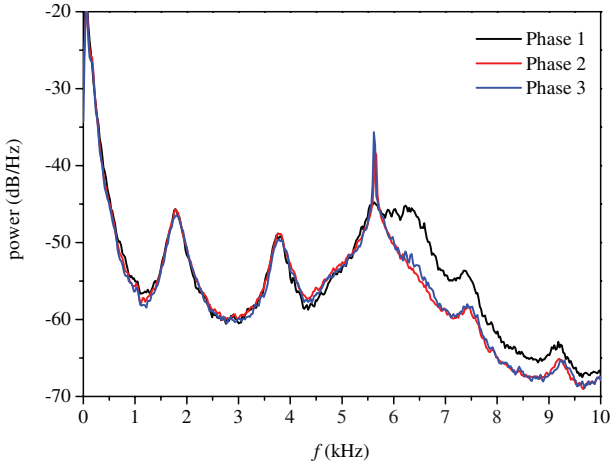

b) Point A: d_o = 7.0 mm, r = 0.67 d_i

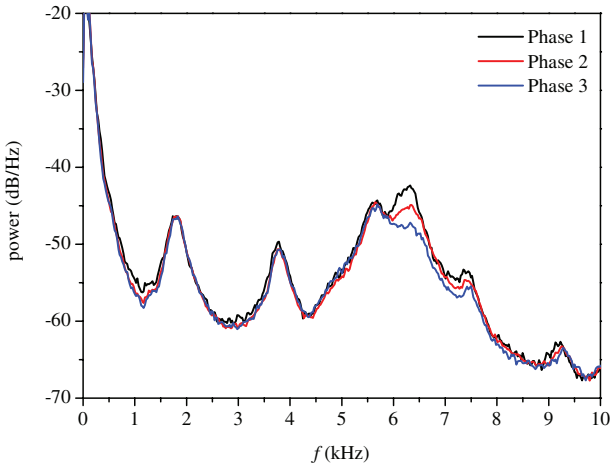

c) Point B: d_o = 7.2 mm

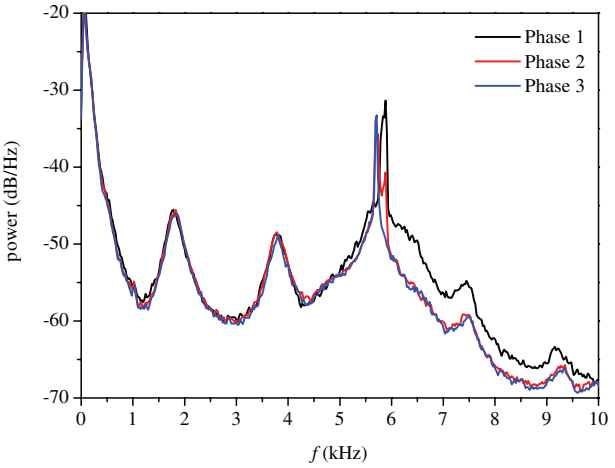

d) Point B: d_o = 7.2 mm, r = 0.67 d_i

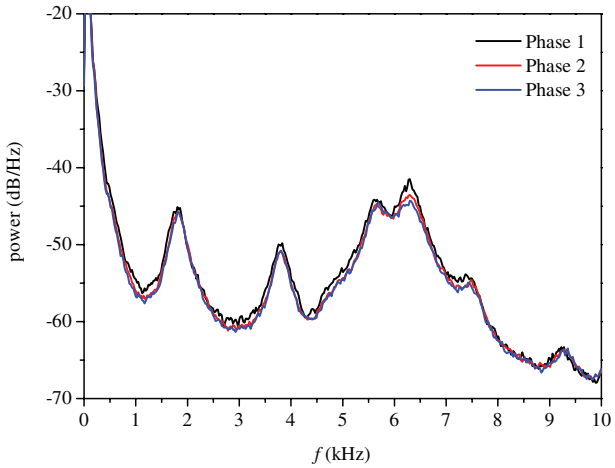

e) Point C: d_o = 7.4 mm

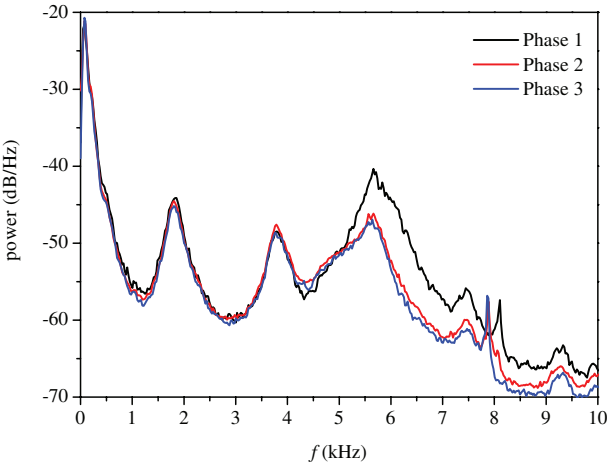

f) Point C: d_o = 7.4 mm, r = 0.67 d_i

Fig. 13 Exemplary power spectra without recess (left) and with recess $r = 0.67 d_i$ (right) at operating points A, B, and C.

Table 3 Resonant frequencies (Hz)

Point	Phase 1	Phase 2	Phase 3	Group
A	——	5640	5640	I
B	5880	5730	5730	I
C	8100	7880	7880	II
D	7850	7750	7750	II
E	——	——	——	——

additional peaks appear or, rather, existing peaks are more pronounced. Several hot runs have been performed using five different injector geometries. Two different groups of resonant frequencies have mainly been detected, as shown in Table 3. The corresponding injection conditions such as velocity ratio, momentum flux ratio, and methane injection velocity for the five different operating points A–E are given in Table 4. The Reynolds numbers of both the liquid oxygen and the methane are given by

$$Re_{\mathrm{LOX}} = \frac{\rho_l \cdot v_l \cdot d_i}{\eta_l} \tag{8}$$

$$Re_{\mathrm{CH_4}} = \frac{\rho_g \cdot v_g \cdot y}{\eta_g} \tag{9}$$

and the methane slot dimension is given by $y = 0.5 \cdot (d_o - d_i) - t$.

No resonant frequencies have been found at very low momentum flux ratios and large methane injection diameters d_o (point E). Because two discrete frequencies have basically been detected, the main physical mechanisms need to be analyzed further. It is assumed that the detected frequencies are also visible in the near-injector flame emission. Because the frame rate was set to 8 kHz to obtain a high optical resolution, no frequencies above 4 kHz can be analyzed.

Table 4 Characteristic numbers at different operating points A–E

	Phase 1	Phase 2	Phase 3
Point A			
P_r	1.17	0.99	0.80
VR	19.33	22.67	28.38
J	16.92	19.68	25.04
$v_{\mathrm{CH_4}}$, m/s	230.19	227.31	230.72
$Re_{\mathrm{CH_4}}$	364,219	312,519	261,856
Re_{LOX}	577,235	493,838	418,079
Point B			
P_r	1.18	1.00	0.81
VR	14.32	16.62	20.76
J	9.88	11.38	14.43
$v_{\mathrm{CH_4}}$, m/s	175.69	173.30	175.53
$Re_{\mathrm{CH_4}}$	361,460	310,836	260,985
Re_{LOX}	645,619	568,153	477,850
Point C			
P_r	1.18	1.00	0.80
VR	12.20	14.26	17.78
J	6.90	8.02	10.16
$v_{\mathrm{CH_4}}$, m/s	150.19	148.35	151.20
$Re_{\mathrm{CH_4}}$	350,715	300,770	251,844
Re_{LOX}	652,118	563,307	486,450
Point D			
P_r	1.17	0.99	0.80
VR	9.82	11.47	14.39
J	4.70	5.45	6.94
$v_{\mathrm{CH_4}}$, m/s	118.35	116.98	119.57
$Re_{\mathrm{CH_4}}$	354,943	306,715	258,184
Re_{LOX}	603,240	525,588	449,756
Point E			
P_r	1.17	0.99	0.80
VR	7.44	8.63	10.83
J	2.69	3.10	3.95
$v_{\mathrm{CH_4}}$, m/s	90.92	89.75	92.06
$Re_{\mathrm{CH_4}}$	344,173	296,367	248,387
Re_{LOX}	635,748	563,821	486,681

As aforementioned, Kim [17] and Kim et al. [18] have simulated the hydrodynamic instabilities inside the recessed region of the SSME main chamber injector. The detected frequencies seem to be of the same order of magnitude ($\approx$8000 Hz) as the measured frequencies of group II shown in Table 3.

VI. Conclusions

The effect of a moderately recessed LOX tube on the flame stabilization in LOX/CH_4 combustion has been investigated experimentally using an optically accessible combustion chamber equipped with a single-shear coaxial injector. High-speed OH emission images have been analyzed using different image-processing methods. It has been shown that a recessed LOX post significantly increases the flame expansion shortly after injection. This effect decreases with an increasing momentum flux ratio J.

Pressure data from several hot runs indicate that the pressure drop across the methane-injection side increases strongly with a recessed LOX tube operated at momentum flux ratios below about 15. The pressure drop across the LOX-injection side always increases by about 10% when using an injector with a recessed LOX tube. Within the present investigation, a recessed LOX tube always led to a smaller combustion roughness.

OH emission images taken at a frame rate of 8 kHz have shown strong hydrodynamic instabilities on the surface of the LOX jet right after injection. In addition, high-frequency dynamic pressure data have mainly indicated two groups of resonant frequencies in the case of a recessed LOX tube. However, additional investigations that include different recess lengths and different LOX post lip sizes are highly recommended to achieve a more detailed understanding of the underlying physical phenomena.

Acknowledgment

The support of the P8 team with the assistance of D. Suslov is greatly acknowledged.

References

[1] Boccaletto, L., "A Comparison Between Two Possible Thermodynamic Schemes for Reusable LOX/LCH_4 Engines," AIAA Paper 2004-3356, 2004.

[2] Singla, G., Scouflaire, P., Rolon, C., Candel, S., Zurbach, S., and Thomas, J. L., "Experiments and Simulations of LOX/CH_4 Combustion at High Pressures," *European Conference for Aerospace Sciences (EUCASS)* [CD-ROM], 2005.

[3] Zong, N., and Yang, V., "Supercritical LOX/Methane Flame Stabilization and Dynamics of a Shear Coaxial Injector," AIAA Paper 2006-760, 2006.

[4] Lux, J., Suslov, D., Bechle, M., Oschwald, M., and Haidn, O., "Investigation Of Sub- and Supercritical LOX/Methane Injection Using Optical Diagnostics," AIAA Paper 2006-5077, 2006.

[5] Salgues, D., Mouis, A.-G., Lee, S.-Y., Kalitan, D., Pal, S., and Santoro, R., "Shear and Swirl Coaxial Injector Studies of LOX/GCH_4 Rocket Combustion Using Non-Intrusive Laser Diagnostics," AIAA Paper 2006-757, 2006.

[6] Gill, G. S., "Liquid Rocket Engine Injectors," NASA SP-8089, 1976.

[7] Kendrick, D., Herding, G., Scouaire, P., Rolon, C., and Candel, S., "Effects of a Recess on Cryogenic Flame Stabilization," *Combustion and Flame*, Vol. 118, No. 3, 1999, pp. 327–339. doi:10.1016/S0010-2180(98)00168-0

[8] Tripathi, A., Juniper, M., Scouaire, P., Durox, D., Rolon, C., and Candel, S., "LOX Tube Recess in Cryogenic Flames Investigated Using OH and H_2O Emission," AIAA Paper 1999-2490, 1999.

[9] Wheeler, D. B., and Kirby, F. M., "High-Pressure LOX/CH_4 Injector Program," NASA CR-161342, 1979.

[10] Juniper, M. P., and Candel, S. M., "The Stability of Ducted Compound Flows and Consequences for the Geometry of Coaxial Injectors," *Journal of Fluid Mechanics*, Vol. 482, May 2003, pp. 257–269. doi:10.1017/S0022112003004075

[11] Hutt, J. J., and Rocker, M., "High-Frequency Injection-Coupled Combustion Instability," *Liquid Rocket Engine Combustion Instability*, edited by V. Yang, and W. Anderson, Vol. 169, Progress in Aeronautics and Astronautics, AIAA, Reston, VA, 1995, pp. 345–355.

[12] Wanhainen, J. P., Parish, H. C., and Conrad, E. W., "Effect of Propellant Injection Velocity on Screech in 20,000-Pound Hydrogen-Oxygen Rocket Engine," NASA TN D-3373, 1966.
[13] Hannum, N. P., Russell, L. M., Vincent, D. W., and Conrad, E. W., "Some Injector Element Detail Effects on Screech in Hydrogen-Oxygen Rockets," NASA TM X-2982, 1974.
[14] Rubinsky, V. R., "Combustion Instability in the RD-0110 Engine," *Liquid Rocket Engine Combustion Instability*, edited by V. Yang, and W. Anderson, Vol. 169, Progress in Aeronautics and Astronautics, AIAA, Reston, VA, 1995, pp. 89–112.
[15] Mayer, W., and Tamura, H., "Propellant Injection in a Liquid Oxygen/Gaseous Hydrogen Rocket Engine," *Journal of Propulsion and Power*, Vol. 12, No. 6, 1996, pp. 1137–1147. doi:10.2514/3.24154
[16] Mayer, W., and Tamura, H., "Flow Visualization of Supercritical Propellant Injection in a Ring LOX/GH_2 Rocket Engine," AIAA Paper 1995-2433, 1995.
[17] Kim, B.-D., "Study of Hydrodynamic Instability of Shear Coaxial Flow in a Recessed Region," Ph.D. Dissertation, Purdue Univ., Purdue, IN, 2002.
[18] Kim, B.-D., Heister, S. D., and Collicott, S. H., "Three-Dimensional Flow Simulations in the Recessed Region of a Coaxial Injector," *Journal of Propulsion and Power*, Vol. 21, No. 4, 2005, pp. 728–742. doi:10.2514/1.12651
[19] Bazarov, V. G., and Yang, V., "Liquid-Propellant Rocket Engine Injector Dynamics," *Journal of Propulsion and Power*, Vol. 14, No. 5, 1998, pp. 797–806. doi:10.2514/2.5343
[20] Oefelein, J., "LES of Supercritical LOX-H_2 Injection and Combustion in a Shear-Coaxial Uni-Element Rocket," AIAA Paper 2003-0479, 2003.
[21] Oefelein, J. C., "Mixing and Combustion of Cryogenic Oxygen-Hydrogen Shear-Coaxial Jet Flames at Supercritical Pressures," *Combustion Science and Technology*, Vol. 178, Nos. 1–3, 2006, pp. 229–252. doi:10.1080/00102200500325322
[22] Ivancic, B., "Untersuchungen zur Strömung und Verbrennung im Einspritzgebiet von LOX/H_2- Raketenbrennkammern," Dr. Dissertation, Inst. für Verbrennungstechnik, Univ. Stuttgart, Stuttgart, Germany, 2001.
[23] Ivancic, B., and Mayer, W., "Time and Length Scales of Combustion in Liquid Rocket Thrust Chambers," *Journal of Propulsion and Power*, Vol. 18, No. 2, 2002, pp. 247–253. doi:10.2514/2.5963
[24] Smith, J. J., "High Pressure LOx/H2 Rocket Engine Combustion," Ph.D. Dissertation, Univ. of Adelaide, Adelaide, Australia, 2007.
[25] Schmidt, R., and Wagner, W., "A New Form of the Equation of State for Pure Substances and its Application to Oxygen," *Fluid Phase Equilibria*, Vol. 19, No. 3, 1985, pp. 175–200. doi:10.1016/0378-3812(85)87016-3
[26] Setzmann, U., and Wagner, W., "A New Equation of State and Tables of Thermodynamic Properties for Methane Covering the Range from the Melting Line to 625 K at Pressures up to 1000 MPa," *Journal of Physical and Chemical Reference Data*, Vol. 20, No. 6, 1991, pp. 1061–1151.
[27] Younglove, B. A., "Thermophysical Properties of Fluids 1: Argon, Ethylene, Parahydrogen, Nitrogen, Nitrogen Triuoride, and Oxygen," *Journal of Physical and Chemical Reference Data*, Vol. 11, No. 1, 1982, pp. 1–354.
[28] Jacobsen, R. T., Leachman, J., Penoncello, S. G., and Lemmon, E. W., "Current Status of Thermodynamic Properties of Hydrogen," *International Journal of Thermophysics*, Vol. 28, No. 3, June 2007, pp. 758–772. doi:10.1007/s10765-007-0226-7
[29] Ostrovskii, Y. I., Butusov, M. M., and Ostrovskaya, G. V., "Gologracheskaya Interferometriya (Holographic Interferometry)," Izdatelstvo Nauka, Moscow, 1977.
[30] Herding, G., Snyder, R., Rolon, C., and Candel, S., "Investigation of Cryogenic Propellant Flames Using Computerized Tomography of Emission Images," *Journal of Propulsion and Power*, Vol. 14, No. 2, 1998, pp. 146–151. doi:10.2514/2.5279
[31] Pham, T. D., "An Image Restoration by Fusion," *Pattern Recognition*, Vol. 34, No. 12, 2001, pp. 2403–2411. doi:10.1016/S0031-3203(00)00164-3
[32] Smith, J. J., Schneider, G., Suslov, D., Oschwald, M., and Haidn, O., "Steady-State High Pressure LOX/H_2 Rocket Engine Combustion," *Aerospace Science and Technology*, Vol. 11, No. 1, 2007, pp. 39–47. doi:10.1016/j.ast.2006.08.007
[33] Smith, J. J., Bechle, M., Suslov, D., Oschwald, M., Haidn, O., and Schneider, G., "Steady-State High Pressure LOx/H2 Rocket Engine Combustion," *European Conference For Aerospace Sciences (EUCASS)* [CD-ROM], 2005.
[34] Nunome, Y., Sakamoto, H., Tamura, H., Kumakawa, A., Amagasaki, S., and Inamura, T., "An Experimental Study of Super-Pulsating Flow on a Shear Coaxial Injector with a Recessed Inner Post," AIAA Paper 2007-5560, 2007.
[35] Sutton, G. P., and Biblarz, O., *Rocket Propulsion Elements*, 7th ed., Wiley, New York, 2001.
[36] Harrje, D. T., and Reardon, F. H., "Liquid Rocket Combustion Instability," NASA SP-194, 1972.
[37] Gordon, S., and McBride, B. J., "Computer Program for Calculation of Complex Chemical Equilibrium Compositions and Applications: Analysis," NASA Ref. Publ. 1311, 1994.
[38] Welch, P., "The Use of Fast Fourier Transform for the Estimation of Power Spectra: A Method Based on Time Averaging Over Short, Modified Periodograms," *IEEE Transactions on Audio and Electroacoustics*, Vol. 15, No. 2, 1967, pp. 70–73. doi:10.1109/TAU.1967.1161901

D. Talley
Associate Editor